EXAFS study of lead-free relaxor ferroelectric BaTi(1-x)Zr(x)O3 at the Zr K-edge

Claire Laulhé, Francoise Hippert, Jens Kreisel, Mario Maglione, Annie Simon, Jean-Louis Hazeman, Vivian Nassif

EXAFS study of lead-free relaxor ferroelectric $BaTi_{1-x}Zr_xO_3$ at the Zr *K* edge

C. Laulhé,[1] F. Hippert,[1] J. Kreisel,[1,*] M. Maglione,[2] A. Simon,[2] J. L. Hazemann,[3] and V. Nassif[4]
[1]*Laboratoire des Matériaux et du Génie Physique (CNRS), Bâtiment INPG-MINATEC, 3 parvis Louis Néel, B.P. 257, F-38016 Grenoble cedex 1, France*
[2]*Institut de Chimie de la Matière Condensée de Bordeaux (CNRS), 87 Avenue A. Schweitzer, F-33608 Pessac, France*
[3]*Laboratoire de Cristallographie (CNRS), 25 rue des Martyrs, BP 166, F-38042 Grenoble cedex 9, France*
[4]*CEA Grenoble, DRFMC/SP2M/NRS, 17 rue des Martyrs, F-38054 Grenoble cedex 9, France*
(Received 19 December 2005; revised manuscript received 11 April 2006; published 17 July 2006)

Extended x-ray absorption fine structure experiments at the Zr *K* edge were carried out on perovskite relaxor ferroelectrics $BaTi_{1-x}Zr_xO_3$ (BTZ) ($x=0.25, 0.30, 0.35$), and on $BaZrO_3$ for comparison. Structural information up to 4.5 Å around the Zr atoms is obtained, revealing that the local structure differs notably from the average $Pm\bar{3}m$ cubic structure deduced from the x-ray diffraction. In particular, our results show that the distance between Zr atoms and their first oxygen neighbors is independent of the Zr substitution rate *x* and equal to that measured in $BaZrO_3$, while the x-ray cubic cell parameter increases linearly with *x*. Furthermore, we show that the Zr atoms tend to segregate in Zr-rich regions. We propose that the relaxor behavior in BTZ could be influenced by the random elastic fields generated by this particular chemical arrangement.

DOI: 10.1103/PhysRevB.74.014106 PACS number(s): 61.10.Ht, 77.80.−e, 77.22.Gm, 77.84.Dy

I. INTRODUCTION

The perovskite-type barium zirconate titanate, $BaTi_{1-x}Zr_xO_3$ (BTZ), has attracted considerable attention as a possible lead-free ferroelectric material to replace the current industry standard lead-based ferroelectrics.[1–6] The particularity of BTZ is the continuous change of its properties from a ferroelectric behavior at low Zr substitution rates to a relaxor ferroelectric (relaxor) behavior at higher substitution rates ($0.25 \leqslant x \leqslant 0.5$).[7] The low substitution regime has been mainly studied for its interest in lead-free ferroelectric memories.[4,5] However, due to the recent report of outstanding electromechanical properties in relaxor-based ferroelectric solid solutions,[8,9] it is rather the relaxor regime of BTZ which currently attracts a large research effort.

Relaxors are characterized by a broad and frequency-dependent dielectric anomaly as a function of temperature, instead of a sharp and frequency-independent divergence as in classical ferroelectrics.[10–14] In a relaxor such as $PbMg_{1/3}Nb_{2/3}O_3$ (PMN), the anomaly surprisingly occurs in a cubic average structure which remains centrosymmetric (nonpolar) at all temperatures. It is generally admitted that the peculiar properties of relaxors are related to the presence of nanoscaled polar regions, due to different cation shifts in different parts of the structure.

Two ingredients are often cited for a relaxor ferroelectric: (i) the presence of Pb^{2+} or Bi^{3+} cations (showing large displacements due to their lone pair) and/or (ii) an aliovalent cationic disorder (generating random local electric fields[15] that break long-range polar correlations). Both are present in the extensively studied model relaxor PMN (e.g., Refs. 16–22). On the other hand, BTZ relaxors present a homovalent Zr^{4+}/Ti^{4+} substitution. It has been proposed that the difference in size of Zr^{4+} and Ti^{4+} cations ($r_{Zr^{4+}}/r_{Ti^{4+}}=1.18$) in BTZ induces random elastic fields.[23] Such fields could affect the displacement of the ferroelectrically active Ti^{4+} ions in their oxygen octahedra; yet it is not known how, and on which scale such random elastic fields build up. The $BaTi_{1-x}Zr_xO_3$ solid solution thus opens an interesting route towards the comprehension of the relaxor behavior, and presents a fundamental interest.[7,24–27] Furthermore, it is intriguing that $PbZr_{1-x}Ti_xO_3$ (PZT) shows no relaxation[28] while BTZ does.

The average crystal structure of the BTZ relaxors ($0.25 \leqslant x \leqslant 0.5$) is cubic (space group $Pm\bar{3}m$) at any temperature.[26] Local distortions away from the ideal cubic structure expected from the observation of the relaxation behavior are evidenced by the observation of a first-order Raman scattering,[24,25] which is forbidden in a perfect primitive cubic structure. However, the latter technique does not reveal the nature of these distortions. The aim of the present study is to determine the local structure and chemical order in BTZ relaxors. For this purpose, we used EXAFS (extended x-ray absorption fine structure) spectroscopy, which is a structural and chemical local probe. This technique has been proven to be a powerful tool in analyzing the local distortions in ferroelectric perovskites (e.g., Refs. 29–33). On the other hand, only a few EXAFS studies have been reported for relaxors.[34–39]

In the case of BTZ, the effect of the substitution of Ti by Zr in the ferroelectric $BaTiO_3$ can be easily studied by EXAFS at the Zr *K* edge. Unfortunately, due to the overlap of the Ti *K* edge with the Ba L_{III} edge, it is very difficult to directly investigate the Ti environment in BTZ, as in $BaTiO_3$.[29,40] In the following, we report an EXAFS study of three BTZ relaxors ($x=0.25$, 0.30, and 0.35) at the Zr *K* edge. The local structure parameters were determined up to distances of 4.5 Å from the Zr atoms, giving information on their local environment up to their fourth neighbors. Hence, the Zr/Ti repartition could be probed, as well as the distortions induced by the presence of Zr atoms. In order to have a proper reference for the understanding of the local Zr environment, we also studied $BaZrO_3$ under the same experimental conditions.

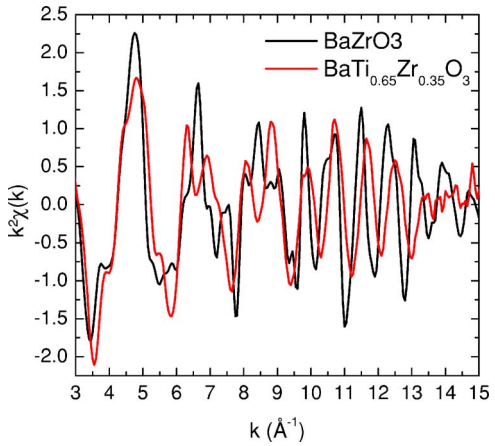

FIG. 1. (Color online) k^2-weighted normalized EXAFS signals for $BaZrO_3$ and $BaTi_{0.65}Zr_{0.35}O_3$ at 300 K.

II. EXPERIMENTAL METHODS

A. Samples and experiments

$BaTi_{1-x}Zr_xO_3$ (x=0.25, 0.30, 0.35, and 1) powders were synthesized by solid state reactions, starting from the appropriate amounts of $BaCO_3$, TiO_2, and ZrO_2 powders and following the method described in Ref. 7. They were then characterized by x-ray diffraction at 300 K. All the powders were found to be single phases within the accuracy of the experiment. The cubic cell parameters are 4.054(1), 4.061(1), 4.072(1), and 4.192(1) *Å* for x values of 0.25, 0.30, 0.35, and 1, respectively.

EXAFS experiments at the Zr K edge (17.998 keV) were carried out on the FAME beamline BM30B at the European Synchrotron Radiation Facility (ESRF). The x-ray absorption coefficient μ was measured in the transmission mode as a function of the incident photon energy E in the range [17.8–19.5 keV], using a Si(220) single crystal monochromator. The samples consisted of pellets made of $BaTi_{1-x}Zr_xO_3$ powders (with a grain size of about 1 μm) mixed with very low-absorbing boron nitride. The effective thickness e of each sample was chosen in such a way that the product μe increases approximately by 1 through the Zr K edge. EXAFS data were collected at room temperature for all samples, as well as at 11 K for $BaZrO_3$ and at 11, 90, and 150 K for $BaTi_{0.65}Zr_{0.35}O_3$.

B. EXAFS data treatment

The scattering of the photoelectron by the neighbors of the central absorbing atom introduces oscillations in the energy dependence of the absorption coefficient $\mu(E)$ after the energy edge. The normalized experimental EXAFS signal is given by $\chi(k)=[\mu(k)-\mu_0(k)]/\Delta\mu_0(k=0)$. μ_0 is the smooth, atomiclike, absorption background, $\Delta\mu_0(k=0)$ is the absorption edge jump, and k is the photoelectron wave number, given by $k=\sqrt{2m_e(E-E_0)/\hbar^2}$ with m_e the electron mass and E_0 the edge energy. In the present work, $\chi(k)$ was extracted from the measured absorption coefficient $\mu(E)$, by using the AUTOBK program.[41] E_0 was taken at the first maximum of the derivative of $\mu(E)$ at the Zr K edge. Two representative examples of normalized k^2-weighted $\chi(k)$ spectra are shown in Fig. 1.

The theoretical EXAFS signal $\chi(k)$ is expressed as a sum of contributions from different paths, each path i corresponding to a given scattering process of the photoelectron:

$$\chi(k) = -S_0^2 \sum_i \frac{N_i A_i(k)}{kR_i^2} e^{-2k^2\sigma_i^2} e^{-2R_i/\lambda(k)} \times \sin[2kR_i + 2\delta_c(k) + \phi_i(k)], \quad (1)$$

where N_i is the degeneracy of path i, R_i its half-length, and $A_i(k)$ its effective scattering amplitude. The Debye-Waller (DW) factor σ_i^2 is the standard deviation of the R_i distance distribution, assumed to be Gaussian. The DW factor takes into account both the thermal disorder and a possible small structural disorder. $\delta_c(k)$ and $\phi_i(k)$ are phase shifts associated with the electron propagating into and out the potentials of the absorbing site and scattering sites, respectively. The other parameters are the photoelectron mean-free path $\lambda(k)$ and an overall amplitude factor S_0^2, close to 1, which accounts for many-electron effects in the excited central atom. Note that Eq. (1) includes both single (back-)scattering (SS) and multiple scattering (MS) processes.[42] For a SS path, N_i is simply the number of chemically identical atoms situated at a given distance R_i from the central atom.

The analysis of EXAFS signals at the Zr K edge was performed in R space after a Fourier transform (FT) of the k^2-weighted $\chi(k)$ in the k range [3.2–14.6 $Å^{-1}$], using a Hanning weight function. The calculated FTs were fitted to the experimental ones using the FEFFIT program.[43] The electronic parameters $A_i(k)$, $\phi_i(k)$, $\delta_c(k)$, and $\lambda(k)$ were calculated for both SS and MS paths with the FEFF8.00 code.[44] The structural parameters R_i, σ_i^2, as well as N_i if unknown, were extracted from the fit as will be described in details in Secs. III B–III D. As customary, an additional parameter ΔE_0 was introduced to account for the small difference between the experimental edge energy E_0 and its calculated value using the FEFF code. The parameter S_0^2 was also refined, the experimental value usually differing from the theoretical one.

III. RESULTS

A. General trends

Examples of the Fourier transforms of the experimental k^2-weighted $\chi(k)$ spectra are shown in Fig. 2. For all studied samples and at all temperatures, the FTs can be readily separated into two contributions, characteristic of the perovskite structure. The first neighbors of a Zr atom are six oxygen atoms (denoted hereafter as O1), which form a regular octahedron in the perfect $Pm\bar{3}m$ perovskite structure. The first contribution to the FT, at R values lower than 2.5 Å, only includes a SS process by one of the O1 atoms. The second contribution, in the R range [2.5–4.5 Å], results both from SS processes where the photoelectron is backscattered by either the second (Ba), third (Zr or Ti), or fourth oxygen (O2) neighbors of the Zr atom, and from several MS processes. Note that due to the k dependence of the phase shifts $\phi_i(k)$ and $\delta_c(k)$, the maxima of the FT modulus occur at distances different from the real ones.

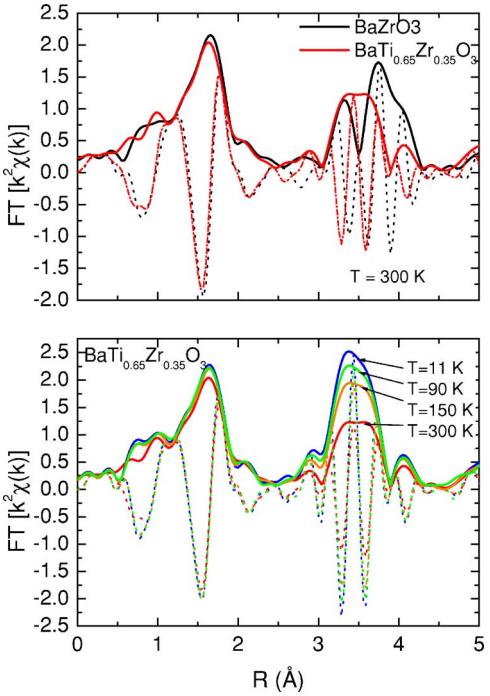

FIG. 2. (Color online) Selected FTs of the k^2-weighted EXAFS signals: $BaZrO_3$ and $BaTi_{0.65}Zr_{0.35}O_3$ at 300 K (top), and thermal evolution in $BaTi_{0.65}Zr_{0.35}O_3$ (bottom). The imaginary part and the modulus of the FTs are plotted as dashed and solid lines, respectively.

Surprisingly, the first peaks of the FTs are nearly identical at 300 K in all relaxor samples *and* in $BaZrO_3$ (see Figs. 2 and 3). The latter suggests very close first neighbor's environment of the Zr atoms, whatever the Zr substitution rate. On the other hand, the FTs of $BaZrO_3$ and BTZ relaxors differ significantly for R values larger than 2.5 Å.

The shape of the FTs suggests an analysis in two steps. Fits of the measured FTs are first performed in the R range related to the Zr first oxygen neighbors (Sec. III B). In a second step, the fitted R range is extended up to 4.5 Å, in order to take into account the further neighbor's contributions (Sec. III C and III D). In BTZ relaxors, one has to take into account both the Zr/Ti substitution and the strong contribution of several MS paths in this R range, which makes the EXAFS analysis complicated. In order to get reference parameters for the analysis of BTZ relaxors, the FT of $BaZrO_3$ is first fitted (Sec. III C). From previous EXAFS studies,[45–47] the local structure of $BaZrO_3$ can be considered as a perfect cubic perovskite structure,[48] identical to the average one deduced from x-ray diffraction (space group $Pm\bar{3}m$).[49,50]

B. Analysis of the first neighbor contribution

We already noted that the backscattering processes between Zr atoms and their first oxygen neighbors (O1) give rise to very similar contributions to the FTs of the EXAFS signals below 2.5 Å, for all samples and at all temperatures (Figs. 2 and 3). From the known structure of $BaZrO_3$, it is then reasonable to assume, as a starting point for the analysis

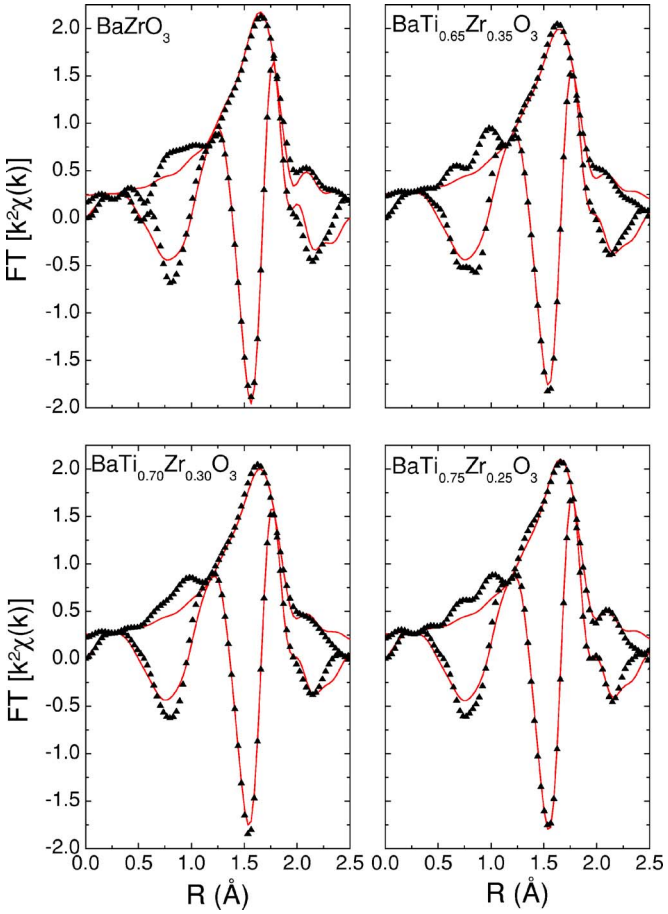

FIG. 3. (Color online) Modulus and imaginary part of the FT of $k^2\chi(k)$ at 300 K. The dots represent measured data and the solid lines their best fit, obtained with the parameters values given in Table I. Measured data for $R<1$ Å are affected by the background subtraction procedure and were excluded from the analysis.

of BTZ relaxors, that the six O1 atoms are located at the same distance from the absorbing Zr atom. Within this hypothesis, only one SS path (denoted hereafter as path 1) contributes in Eq. (1) for the considered R range. The fitted parameters are, for each sample, the Zr-O1 distance R_1, the associated DW factor σ_1^2, and ΔE_0. The number of O1 neighbors, N_1, is fixed to 6. The analysis of the EXAFS data for $BaZrO_3$ at 11 and 300 K allows us to determine a S_0^2 value equal to 1 ± 0.07. This parameter was then fixed to 1 for all the further analysis. The EXAFS oscillations were refined in the R range [1.14–2.33 Å]: the data for R lower than 1 Å are affected by the background subtraction procedure[41] and had to be excluded from the fit. Fits of good quality could be obtained, with reliability factors less than 1%, for all samples at all temperatures (Fig. 3 and Table I).

In $BaTi_{0.65}Zr_{0.35}O_3$ and $BaZrO_3$ samples, no significant temperature dependence of the Zr-O1 distance is detected, within the experimental accuracy of the EXAFS technique. More surprisingly, the Zr-O1 distance hardly varies with the Zr substitution rate x, and keeps values very close to that found in $BaZrO_3$.

The refined values of the σ_1^2 DW factors in $BaZrO_3$ at 11 and 300 K are in good agreement with those reported in Ref.

TABLE I. Structural parameters deduced from the EXAFS analysis in the R range [1.14–2.33 Å], for $BaZrO_3$ and BTZ relaxors. R_1 is the length of the bond between an absorbing Zr atom and its first oxygen neighbor, and ${\sigma_1}^2$ the associated Debye-Waller factor. ${\chi_v}^2$ and RF are the reduced chi-squared and the reliability factor of the fit. The ${\chi_v}^2$ were calculated with a root mean squared value of random fluctuations of 0.85×10^{-3} for all samples, except for $BaZrO_3$ at 11 K: 1.92×10^{-3}. Three parameters were refined on 10.02 independent data points. The uncertainties are of the order of ±0.01 Å and ±0.0004 Å^2 for R_1 and ${\sigma_1}^2$, respectively. The energy shift ΔE_0 was found equal to 1.4±0.8 eV for all fits.

Sample	T (K)	R_1 (Å)	${\sigma_1}^2$ (Å^2)	${\chi_v}^2$	RF factor (%)
$BaZrO_3$	300	2.11	0.0039	12	0.61
	11	2.11	0.0029	3	0.62
$BaTi_{0.65}Zr_{0.35}O_3$	300	2.10	0.0048	8	0.58
	150	2.10	0.0038	8	0.46
	90	2.10	0.0038	16	0.96
	11	2.10	0.0035	9	0.48
$BaTi_{0.70}Zr_{0.30}O_3$	300	2.10	0.0048	8	0.55
$BaTi_{0.75}Zr_{0.25}O_3$	300	2.10	0.0043	7	0.47

47. In BTZ relaxors, systematically higher ${\sigma_1}^2$ values are obtained. From the definition of the DW factor, this increase depicts either a stronger static disorder, or enhanced vibration amplitudes (associated with a decrease of the Zr-O1 bond stiffness). As a matter of fact, the static and dynamic contributions can be separated, by analyzing the thermal evolution of the measured DW factor. In the absence of a static disorder, the DW factor only accounts for thermal vibrations and can be written, in the Einstein model, as

$$\sigma^2_{i\ therm}(T) = \frac{\hbar^2}{2k_B M_R \theta_E} \coth\left(\frac{\theta_E}{2T}\right), \qquad (2)$$

where k_B is the Boltzmann constant and M_R the reduced mass of all atoms involved in the scattering path. The Einstein temperature θ_E, characterizing the bond strength, increases with the bond stiffness. Given our hypothesis of a perfect $Pm\bar{3}m$ perovskite local structure in $BaZrO_3$, the two ${\sigma_1}^2$ values measured at 11 and 300 K in this sample were fitted to Eq. (2). An Einstein temperature of 606±14 K was then obtained for the Zr-O1 bond. In $BaTi_{0.65}Zr_{0.35}O_3$, the thermal evolution of ${\sigma_1}^2$ is consistent with the same θ_E value, provided that a constant $\Delta{\sigma_1}^2 = +0.0007$ Å^2 is added to Eq. (2) (Fig. 4). This result gives evidence for the existence of a static distribution of the Zr-O1 distances in $BaTi_{0.65}Zr_{0.35}O_3$, which is temperature-independent within the experimental accuracy. The full width at half maximum of a Gaussian distribution of distances would be equal to $2\sqrt{2\ln 2\Delta{\sigma_1}^2} = 0.06$ Å. This small value justifies *a posteriori* the use of only one SS path in Eq. (1), the DW factor ${\sigma_1}^2$ taking into account the small disorder that cannot be resolved in R space.

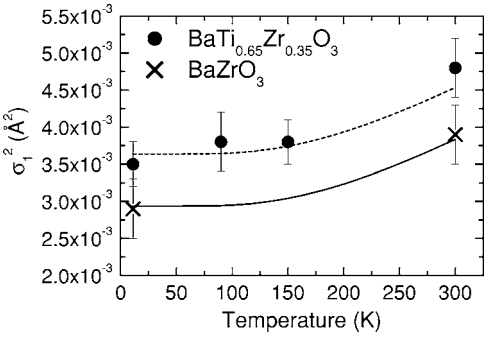

FIG. 4. Thermal evolution of the measured DW factor for the Zr-O1 bond (symbols). The solid line represents Eq. (2) with $\theta_E = 606$ K. The dashed line corresponds to the same function shifted by 0.0007 Å^2.

The mean square deviation of the R_i distance linked to a static disorder, $\Delta\sigma_i^2$, is intended to describe a Gaussian static distribution of distances in Eq. (1), with $\sigma_i^2 = \sigma^2_{i\ therm}(T) + \Delta\sigma_i^2$. However, a measured nonzero value of $\Delta\sigma_i^2$ can describe other distance distributions (discrete or continuous), provided their width remains small. In the present case, the distribution of the Zr-O1 distances could be due to a distortion of the ZrO_6 units, coming from the Zr/Ti chemical disorder, and/or to a displacement of Zr atoms in their octahedral cages. To evaluate the magnitude of such a displacement, we calculated the FT of the EXAFS signals for Zr atoms in a perfect octahedron, weakly displaced either along the [100], [110], or [111] cubic axis. We then performed fits on the calculated signals in the same conditions as described above for the measured signals. From these simulations, we conclude that the refined DW factors presented in Table I for $BaTi_{0.65}Zr_{0.35}O_3$ could correspond to a Zr displacement of 0.07 Å, in any of the three directions cited above.

In conclusion, the length and strength of the bond between a Zr atom and its first oxygen neighbor are found to be independent of the Zr substitution rate in $BaTi_{1-x}Zr_xO_3$ samples. Only a small temperature-independent distribution of the Zr-O1 distances is detected in $BaTi_{0.65}Zr_{0.35}O_3$, in opposition to the single distance in the regular octahedron present in $BaZrO_3$. These fluctuations of the Zr-O1 distance can be due to Zr displacements in their octahedra, but can also result from distortions of the ZrO_6 octahedra induced by the Zr/Ti chemical disorder. Note that a static distribution of Zr-O1 distances is also expected in the two other relaxor samples, $BaTi_{0.70}Zr_{0.30}O_3$ and $BaTi_{0.75}Zr_{0.25}O_3$, from the ${\sigma_1}^2$ values measured at 300 K and by analogy with the case of $BaTi_{0.65}Zr_{0.35}O_3$.

C. Analysis of the further neighbor contribution: $BaZrO_3$

For R values up to 4.5 Å, the FT of the EXAFS signal involves scattering processes beyond the first oxygen neighbors. The amplitudes and phases of all the possible paths have been calculated by using the FEFF8.00 code, for an atomic cluster of 145 atoms representative of the $BaZrO_3$ $Pm\bar{3}m$ perovskite structure. The scattering processes with

TABLE II. SS and MS paths used to analyze $BaZrO_3$ EXAFS data. N_i is the degeneracy of path i, and R_i its half-length, expressed as a function of R_1 assuming an ideal perovskite structure. Zr_c is the central absorbing Zr atom. The O1 and O1′ atoms are located on opposite sides of the Zr_c atom, between Zr_c and one of its six Zr third neighbors.

Index	Scattering process	N_i	R_i	σ_i^2
1	$Zr_c \rightarrow O1 \rightarrow Zr_c$	6	R_1	σ_1^2
2	$Zr_c \rightarrow Ba \rightarrow Zr_c$	8	$\sqrt{3}R_1$	σ_2^2
3	$Zr_c \rightarrow Zr \rightarrow Zr_c$	6	$2R_1$	σ_3^2
4	$Zr_c \rightarrow O1' \rightarrow O1 \rightarrow Zr_c$	6	$2R_1$	σ_4^2
5	$Zr_c \rightarrow Zr \rightarrow O1 \rightarrow Zr_c$	12	$2R_1$	σ_3^2
6	$Zr_c \rightarrow O1' \rightarrow Zr_c \rightarrow O1 \rightarrow Zr_c$	6	$2R_1$	σ_4^2
7	$Zr_c \rightarrow O1 \rightarrow Zr_c \rightarrow O1 \rightarrow Zr_c$	6	$2R_1$	$2\sigma_1^2$
8	$Zr_c \rightarrow O1 \rightarrow Zr \rightarrow O1 \rightarrow Zr_c$	6	$2R_1$	σ_3^2
9	$Zr_c \rightarrow O1 \rightarrow Ba \rightarrow Zr_c$	48	$\frac{1+\sqrt{2}+\sqrt{3}}{2}R_1$	σ_9^2
10	$Zr_c \rightarrow O2 \rightarrow Zr_c$	24	$\sqrt{5}R_1$	σ_{10}^2

relative weight lower than 2.5% have been neglected. The single backscattering processes on the second (Ba), third (Zr), and fourth (O2) neighbors of the Zr central atom must be considered, as well as several collinear MS paths and only two nonlinear MS paths. One of the two latter paths involves Ba atoms. The other one is a triple scattering path within the ZrO_6 octahedron, which corresponds to a R range between the two main peaks of the FTs. We verified that it does not affect the fit, and did not consider it further. The retained paths for the EXAFS analysis are listed in Table II. Note that the half-lengths of all the collinear MS paths are equal to the Zr-Zr distance. As a consequence, these MS paths contribute to the FT in the same R range as the single backscattering path by a Zr atom, which makes the analysis complex.

Assuming a perfect $Pm\bar{3}m$ cubic structure, all N_i are known and the R_i parameters for the ten paths can be expressed as a function of R_1, the distance between the central absorbing Zr atom and O1 (see Table II). The number of σ_i^2 parameters needed could be decreased using the expression of the DW factor:[42]

$$\sigma_i^2 = \frac{1}{4}\left\langle \left[\sum_j (\vec{u}_{j+1} - \vec{u}_j) \cdot \vec{R}_{jj+1} \right]^2 \right\rangle_t, \qquad (3)$$

where t is the time, j represents an atomic site of the scattering path i, $\vec{u}_j$ is the displacement vector of the j atom, and $\vec{R}_{jj+1}$ is the directing unit vector between j and $j+1$ atoms at equilibrium. The resulting relations between the σ_i^2 parameters in $BaZrO_3$ are given in Table II. For the fit of the measured FT, in the R range [1.14–4.52 Å], seven parameters were then refined: ΔE_0, R_1, σ_2^2, σ_3^2, σ_4^2, σ_9^2, and σ_{10}^2. Although they have already been determined in Sec. III B, R_1 and the strongly correlated parameter ΔE_0 were refined,[51] all distances up to 4.5 Å being functions of R_1. On the other hand, the S_0^2 and σ_1^2 parameters were fixed to the previously refined values. The obtained parameters at 11 and 300 K are presented in Table III. During the refinement process, the σ_4^2 and σ_9^2 values were found to have no influence on the RF factor. These two DW factors are related to paths 4, 6, and 9, which give rise to very large, and relatively weak contributions in R space. Consequently, σ_4^2 and σ_9^2 values do not affect significantly the amplitude and shape of these contributions and cannot be precisely determined, so that they are not given in Table III.

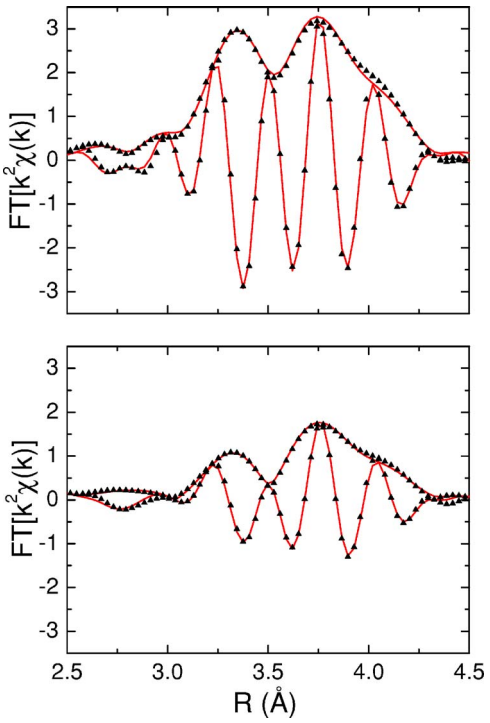

FIG. 5. (Color online) Modulus and imaginary part of the FT of $k^2\chi(k)$ for $BaZrO_3$, at 11 K (top) and 300 K (bottom). The dots represent measured data and the solid lines their best fit. The fit parameters are given in Table III.

TABLE III. Structural parameters deduced from the EXAFS analysis in the R range [1.14–4.52 Å], for $BaZrO_3$. The parameters have already been defined in Tables I and II. Seven parameters were refined on 24.16 independent data points. The uncertainties are of the order of ±0.01 Å for R_1, ±0.0003 Å^2 for σ_2^2 and σ_3^2, and ±0.003 Å^2 for σ_{10}^2. ΔE_0 was found equal to 0.0±0.5 eV for both fits.

	R_1 (Å)	σ_2^2 (Å^2)	σ_3^2 (Å^2)	σ_{10}^2 (Å^2)	χ_ν^2	RF factor (%)
300 K	2.10	0.0072	0.0048	0.013	9	1.04
11 K	2.10	0.0026	0.0025	0.006	4	1.01

The calculated FTs are in very good agreement with the measured ones (Fig. 5). The DW factors for the Zr-Ba (σ_2^2), Zr-Zr (σ_3^2), and Zr-O_2 (σ_{10}^2) bonds are consistent with those reported in Ref. 47. Their thermal evolution was fitted to Eq. (2), resulting in Einstein temperatures equal to 194±8 K, 263±10 K, and 296±50 K for the Zr-Ba, Zr-Zr, and Zr-O2 bonds, respectively.

The analysis of the EXAFS oscillations in $BaZrO_3$ gives information on the relative contributions of the different paths to the FTs in the *R* range [2.5–4.5 Å], which will help us to analyze BTZ samples (see Fig. 6). Only the backscattering path on Ba atoms (path 2 in Table II) contributes in the *R* range [3.0–3.6 Å], which allows us a precise determination of the Zr-Ba distance and the associated DW factor. The contributions in the *R* range [3.6–4.2 Å] mainly arise from the MS linear paths that involve the third neighbor Zr atoms (paths 5 and 8 in Table II). The backscattering path on Zr atoms (path 3) also contributes in the same *R* range, but it is much less important. The remaining MS paths (paths 4, 6, 7, and 9 in Table II) correspond to weak contributions to the FTs, but it is necessary to take them into account in order to obtain good quality fits. The DW factors of paths 4, 6, and 9 were shown to have no influence on the fit. Finally, the backscattering path on O2 atom (path 10) contributes over a very large *R* range [3–4.6 Å]. It is then compulsory to keep this path in the analysis, as it cannot be separated from the other contributions to the FTs.

D. Analysis of the further neighbor contribution: BTZ relaxors

In the following analysis, we shall introduce two different models of the local structure in BTZ relaxors. In a first step, we show that a model with aligned Zr, O1, and (Zr/Ti) atoms in the perovskite structure cannot account for the measured EXAFS signals. In a second step, we introduce a buckling angle for the Zr-O1-(Zr/Ti) bonds.

1. Basic model for the BTZ analysis

The $BaZrO_3$ model (see Sec. III C) is used as a starting point to analyze BTZ samples. To take into account the Ti

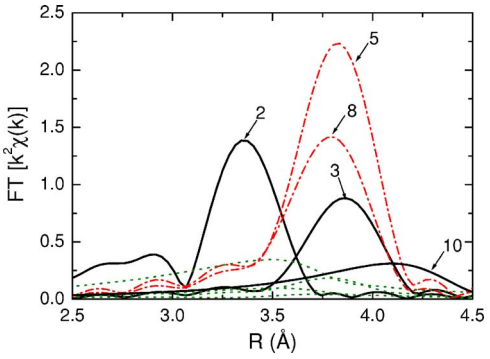

FIG. 6. (Color online) Modulus of the FT of the individual contributions to $k^2\chi(k)$, in $BaZrO_3$ at 300 K. SS paths, MS paths within Zr_c octahedra, and MS paths outside Zr_c octahedra are represented as solid, dash-dotted, and dotted lines, respectively. Numbers correspond to the path indexes of Table III.

third neighbors, we also calculated the amplitudes and phases of the scattering paths within a hypothetical cluster of $BaTiO_3$ in the $Pm\bar{3}m$ cubic perovskite structure, with a single Zr impurity as the absorbing atom. For the paths that do not involve Ti atoms, the calculated amplitude and phase remain strictly identical to those calculated for the $BaZrO_3$ structure. Thus, we only consider three extra paths 3′ ($Zr_c \rightarrow Ti \rightarrow Zr_c$), 5′ ($Zr_c \rightarrow Ti \rightarrow O1 \rightarrow Zr_c$), and 8′ ($Zr_c \rightarrow O1 \rightarrow Ti \rightarrow O1 \rightarrow Zr_c$), in addition to those presented in Table II. The *k* dependence of these path amplitudes differs significantly from that of the corresponding paths 3, 5, and 8 of the $BaZrO_3$ model. Thus, the EXAFS technique allows the refinement of structural parameters for Zr and Ti atoms with limited correlations effects, despite similar Zr-Zr and Zr-Ti distances. A new parameter N_{Zr} has to be introduced, which is the average number of Zr third neighbors of the central atom Zr_c. The degeneracy of paths 3, 5, and 8 is then multiplied by $N_{Zr}/6$, and that of paths 3′, 5′, and 8′ by $(6-N_{Zr})/6$. A unique $\sigma_{3'}^2$ parameter is attached to the paths 3′, 5′ and 8′, according to Eq. (3).

Zr atoms are larger than Ti ones, so that they likely cause local distortions in the $BaTiO_3$ matrix. This difference in size is taken into account by introducing independent Zr-O1, Zr-Ba, Zr-Ti, and Zr-O2 distances. The O1 atoms lying between Zr_c and (Zr/Ti) atoms in this first model, the Zr-Zr and Ti-O1 distances are defined using the expressions $d_{Zr\text{-}Zr}=2d_{Zr\text{-}O1}$ and $d_{Ti\text{-}O1}=d_{Zr\text{-}Ti}-d_{Zr\text{-}O1}$. The DW factors σ_4^2 and σ_9^2 were fixed to the same values as in $BaZrO_3$, since they are not expected to affect the fit (see Sec. III C). Furthermore, the relations between the DW factors presented in Table II remain correct, so that only σ_2^2, σ_3^2, $\sigma_{3'}^2$, and σ_{10}^2 DW factors were refined. The Zr-O1 distance (R_1) and σ_1^2, as well as ΔE_0 and S_0^2, were fixed to the values refined in the *R* range [1.14–2.33 Å] (see Table I).

Within this model, the fitting procedure over the *R* range [1.14–4.52 Å] yields nonphysical values of the σ_3^2 and $\sigma_{3'}^2$ parameters (0.033 and −0.0008, respectively, at 11 K). In fact, the calculated contribution of paths linked to Zr atoms (paths 3, 5, and 8 in Table II) are completely damped (see top of Fig. 7). Only paths involving Ti atoms then contribute to the calculated signal, in the *R* range [3.4–3.9 Å]. Fixing σ_3^2 to its value in $BaZrO_3$ made impossible a good agreement between calculated and experimental signals. In particular, the shift of the FT's imaginary part in the *R* range [3.6–3.9 Å] indicates an overestimated Zr-Zr distance (see bottom of Fig. 7). Hence, we deduce that $d_{Zr\text{-}Zr}$ must be smaller than $2d_{Zr\text{-}O1}$.

2. Determination of the buckled local structure in BTZ relaxors

With the hypothesis of aligned Zr_c, O1, and Zr atoms being not valid in BTZ samples, a new model has to be built, where the O1 atoms are no longer aligned with Zr ones. In order to get all different possible configurations, one can introduce two mean buckling angles Θ_{Zr} and Θ_{Ti} defined as $180°-\widehat{ZrO1Zr}$ and $180°-\widehat{ZrO1Ti}$, respectively. All the possible paths and their parameters were calculated in the preceding $BaZrO_3$ and $BaTiO_3$ clusters, moving the O1 atoms

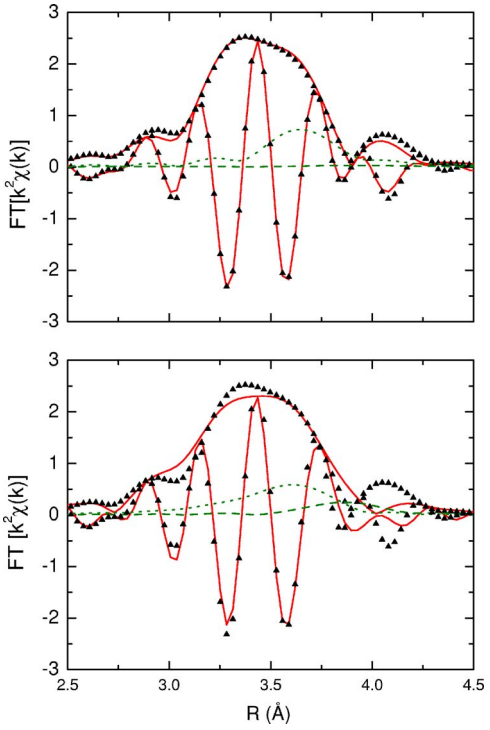

FIG. 7. (Color online) Modulus and imaginary part of the FTs of the observed (dots) and refined (solid line) $k^2\chi(k)$ for $BaTi_{0.65}Zr_{0.35}O_3$ at 11 K. The modulus of the FT for paths 3 (dashed line) and 3′ (dotted line), which describe the backscattering on Zr and Ti atoms, respectively, are also represented. The fits were obtained in the hypothesis of aligned Zr, O1, and (Zr/Ti) atoms. Top: the path 3 is completely damped by a nonphysical, huge σ_3^2 DW factor. Bottom: σ_3^2 is fixed to its value in $BaZrO_3$, i.e., 0.0020 Å^2. The calculated imaginary part is then shifted towards high R values in the R range [3.7–3.9 Å], where the path 3 now contributes. The latter clearly indicates an overestimated $d_{Zr\text{-}Zr}$ distance.

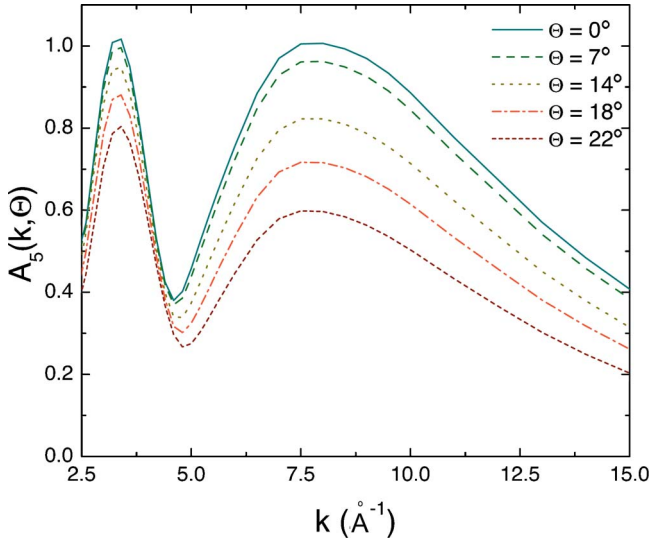

FIG. 8. (Color online) Evolution of the focusing path amplitudes with increasing values of the buckling angle Θ: example of path 5.

out of their collinear sites with varying values of the buckling angle Θ. The only effect of the O1 atom displacements is the damping of the amplitudes of the MS paths in which these atoms play a focusing role, i.e., paths 5, 5′, 8, and 8′ (Table II). As an example, we show the evolution of the amplitude of path 5 as a function of Θ on Fig. 8. This evolution can be expressed by expending the scattering amplitude of the focusing paths about $\Theta=0$:

$$A(k,\Theta) \approx A(k,0)[1 - b(k)\Theta^2]^n, \qquad (4)$$

where n is the number of scattering processes by the off-centered focusing atom (O1).[52] For each of the paths 5, 5′, 8, and 8′, the coefficients $b(k)$ were determined for various buckling angles and averaged. Equation (4) is found to be correct for the buckling angles' values below 20°.

The expressions for Zr-Zr and Ti-O1 distances are now given by $d_{Zr\text{-}Zr}=2d_{Zr\text{-}O1}\cos(\Theta_{Zr}/2)$, and $d_{Ti\text{-}O1} = \sqrt{d_{Zr\text{-}Ti}^2 - d_{Zr\text{-}O1}^2 \sin^2\Theta_{Ti}} - d_{Zr\text{-}O1}\cos\Theta_{Ti}$, from which the lengths of paths 1–8 can be easily derived. The path length R_9 splits into several different values, due to the misalignment of the O1 oxygen atoms. This effect can be modeled by an increase of the corresponding DW factor σ_9^2, but we already showed that this parameter does not affect the fit quality. Thus, we determined the mean distance R_9 with the expression given in Table II, using the the σ_9^2 value of $BaZrO_3$. The length of path 10 splits as well, depending on the size and shape of the octahedra next to the central one Zr_cO_6. With this information being out of the scope of this study, we assigned to this path an average value of the Zr-O2 distances, R_{10}. In that case σ_{10}^2 is expected to take into account both thermal and static disorders. In the absence of an adequate model for the O2 repartition, the values obtained for R_{10} and σ_{10}^2 will not be interpreted. Concerning the DW factors, the linearity of paths 5, 5′, 8, and 8′ is broken by the off-centering of O1 atoms with respect to Zr-(Zr/Ti) bonds, so that the relations $\sigma_5^2=\sigma_8^2=\sigma_3^2$ and $\sigma_5'^2=\sigma_8'^2=\sigma_{3'}^2$ are no longer exact. However, we postulated their validity for the buckled paths, in order to limit the number of free parameters. The buckling angles Θ_{Zr} and Θ_{Ti} were determined separately, as preliminary fits using the same buckling angle for both Zr_c-O1-Zr and Zr_c-O1-Ti bonds did not yield a good agreement between experimental and calculated signals (see Fig. 9). Ten parameters were then refined: R_2, $R_{3'}$, R_{10}, N_{Zr}, Θ_{Zr}, Θ_{Ti}, σ_2^2, σ_3^2, $\sigma_{3'}^2$, and σ_{10}^2. The σ_3^2 and $\sigma_{3'}^2$ parameters were found to reach very low (nonphysical) values when not fixed. Like N_{Zr}, Θ_{Ti}, and Θ_{Zr}, these two DW factors determine the signal amplitude in the R range [3.4–3.9 Å]. Strong correlation effects exist between these five parameters and various sets of their values give rise to similar, very good fits. To go further in the analysis, we assume that σ_3^2 and $\sigma_{3'}^2$ in BTZ relaxors are equal to σ_3^2 in $BaZrO_3$, which is determined for all temperatures using Eq. (2) with the Einstein temperature of 263 K reported in Sec. III C. Values of refined parameters in this hypothesis are presented in Table IV and fits are shown in Fig. 10 for the three BTZ relaxors. The fits are not very sensitive to the variations of Θ_{Ti} in the range [0°–10°]. Θ_{Ti} values larger than 10° are excluded since they do not yield satisfactory agreements.

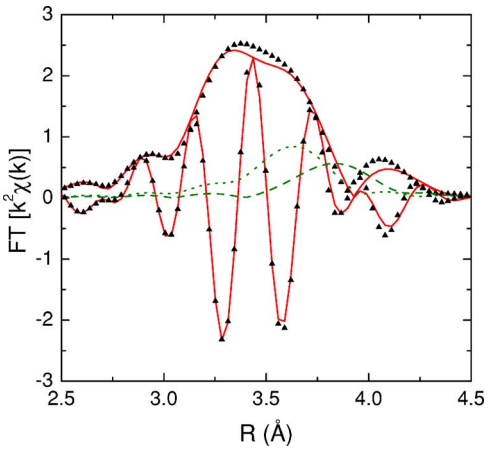

FIG. 9. (Color online) Modulus and imaginary part of the FTs of the observed (dots) and refined (solid line) $k^2\chi(k)$ for $BaTi_{0.65}Zr_{0.35}O_3$ at 11 K. The modulus of the FT for paths 3 (dashed line) and 3′ (dotted line), which describe the backscattering on Zr and Ti atoms, respectively, are also represented. We show the best fit obtained in the hypothesis of a single buckling angle for Zr_c-O1-Zr and Zr_c-O1-Ti bonds, for reasonable values of ${\sigma_3}^2$ and ${\sigma_{3'}}^2$ parameters. The missing amplitude in the R-range [3.3–3.7 Å], characteristic of the path 3′, indicates an overestimated buckling angle for the Ti bonds.

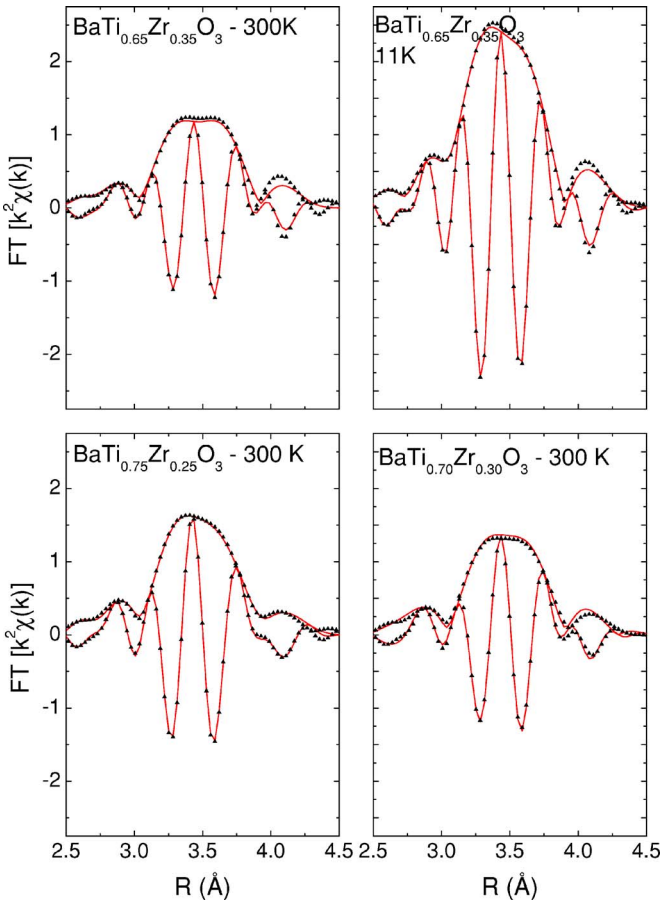

FIG. 10. (Color online) Modulus and imaginary part of the FT of $k^2\chi(k)$ at either 11 or 300 K, for BTZ samples. The dots represent measured data and the solid lines their best fit, obtained with the parameters values given in Table IV.

Note that the Zr-Ba distance and the associated DW factor ${\sigma_2}^2$ are accurately defined, the contribution of path 2 to the FTs being well separated from the others.

One needs to estimate the consequences of fixing ${\sigma_3}^2$ and ${\sigma_{3'}}^2$ for the analysis of BTZ relaxors. For this purpose, we performed several fits for various, not necessarily equal, values of ${\sigma_3}^2$ and ${\sigma_{3'}}^2$, in a range of ±0.0010 Å^2 around the ${\sigma_3}^2$ value in $BaZrO_3$. The Θ_{Zr}, N_{Zr}, and $R_{3'}$ values were found to vary by ±1.5°, ±0.2, and ±0.01 Å, respectively. Furthermore, the refined values of Θ_{Zr} being at the limit of the validity range of Eq. (4), one expects an error of ±1° on its determination. The uncertainties given in Table IV are those determined by the FEFFIT code, augmented by the preceding amounts. Note that in the case of $BaTi_{0.65}Zr_{0.35}O_3$, the refined value of N_{Zr} is found to be independent of the temperature, as it should be. This confirms *a posteriori* that the hypothesis of an identical thermal evolution of ${\sigma_3}^2$ and ${\sigma_{3'}}^2$ in BTZ samples and ${\sigma_3}^2$ in $BaZrO_3$ is reasonable.

TABLE IV. Structural parameters deduced from the EXAFS analysis in the R range [1.14–4.52 Å], for BTZ relaxors. The path half-lengths are denoted R_i, and the associated DW factors ${\sigma_i}^2$. Θ_{Zr} is the buckling angle of the Zr-O1-Zr bonds, defined as $180°-\widehat{ZrO1Zr}$, and N_{Zr} the mean number of Zr third neighbors of the Zr_c atom. R_3 is deduced from R_1 (Table I) and Θ_{Zr}. Ten parameters were refined on 24.16 independent data points. The uncertainties are of the order of ±0.006 Å, ±0.0004 Å^2, ±5°, ±0.04 Å, ±0.02 Å, ±0.04 Å, ±0.005 Å^2, and ±1.0 for R_2, ${\sigma_2}^2$, Θ_{Zr}, R_3, $R_{3'}$, R_{10}, ${\sigma_{10}}^2$, and N_{Zr}, respectively.

Sample	T (K)	R_2 (Å)	${\sigma_2}^2$ (Å^2)	Θ_{Zr} (°)	R_3 (Å)	$R_{3'}$ (Å)	R_{10} (Å)	${\sigma_{10}}^2$ (Å^2)	N_{Zr}	${\chi_\nu}^2$	RF factor (%)
$BaTi_{0.65}Zr_{0.35}O_3$	300	3.557	0.0070	18	4.15	4.07	4.61	0.018	3.4	8	1.09
	150	3.554	0.0048	17	4.15	4.06	4.60	0.014	3.4	10	0.81
	90	3.556	0.0041	19	4.15	4.07	4.60	0.012	3.4	11	0.80
	11	3.554	0.0037	18	4.14	4.06	4.60	0.012	3.3	8	0.51
$BaTi_{0.70}Zr_{0.30}O_3$	300	3.553	0.0068	19	4.16	4.07	4.60	0.019	3.1	7	0.84
$BaTi_{0.75}Zr_{0.25}O_3$	300	3.544	0.0060	20	4.16	4.07	4.60	0.015	2.7	76	0.49

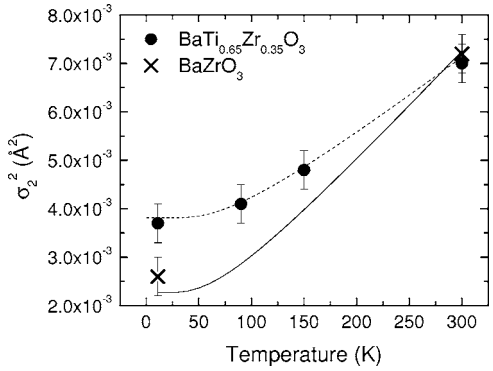

FIG. 11. Thermal evolution of the measured DW factor for the Zr-Ba bond (symbols). The solid line represents Eq. (2) with θ_E =194 K. The dashed line corresponds to the same equation with θ_E=231 K, and shifted by 0.0019 Å^2.

3. Fit results

For all the relaxor samples investigated, the refined values of the buckling angle Θ_{Zr} range from 18° to 20°. With Θ_{Ti} being smaller (less than 10°), the ZrO_6 octahedra are, therefore, distorted differently depending on the type of the third neighbors (Zr or Ti) of the Zr central atom.

In BTZ relaxors, the existence of a nearly constant buckling angle as a function of the Zr substitution rate x, together with the invariant Zr-O1 distance (Sec. III B) result in a Zr-Zr distance of the order of 4.15 Å, which hardly varies with x. Of course, the Zr-Zr distance is smaller in BTZ samples than in $BaZrO_3$, since the oxygen atoms are aligned with the Zr-Zr bonds in the latter compound. The Zr-Ti distance (4.07 Å) does not change with x, and is found to be significantly smaller than the Zr-Zr distance. The Zr-Ba distance, on its turn, increases with x. From the Zr-Ti distance and the buckling angle of the Zr-O1-Ti bond, we can derive the Ti-O1 distance value at 300 K in BTZ relaxors, which is of the order of 1.98 Å. This corresponds to the shortest Ti-O distance in the quadratic $BaTiO_3$ at 300 K.[53]

We now consider the temperature dependence of σ_2^2 in the $BaTi_{0.65}Zr_{0.35}O_3$ sample. As shown in Fig. 11, it can be described following Eq. (2) with an Einstein temperature equal to 231±4 K, instead of 194±8 K in $BaZrO_3$. This result indicates an increase of Zr-Ba bond strength with increasing Ti content. In addition, a constant $\Delta\sigma_2^2$ =0.0019 Å^2 must be added to Eq. (2), revealing the presence of a static disorder. The full width at half maximum of the corresponding Gaussian distance distribution would be equal to $2\sqrt{2\ln 2\Delta\sigma_2^2}$=0.10 Å. However, let us remind the reader that other distance distributions can be expected (see Sec. III B). The possible distribution of the Zr-Zr and Zr-Ti bond lengths is out of the scope of this study, since σ_3^2 and $\sigma_{3'}^2$ parameters had to be fixed during the refinement process.

The mean number of Zr third neighbors around a Zr atom N_{Zr} brings information on the distribution of the Zr and Ti atoms in BTZ relaxor samples. N_{Zr} is found to be equal to 2.7, 3.1, and 3.4 in $BaTi_{0.75}Zr_{0.25}O_3$, $BaTi_{0.70}Zr_{0.30}O_3$, and $BaTi_{0.65}Zr_{0.35}O_3$ samples, respectively. Despite the large uncertainty attached to N_{Zr} (±1.0), the measured values are higher than those expected for a random distribution of Zr and Ti atoms: 1.5, 1.8, and 2.1. This observation indicates a tendency of Zr atoms to segregate in Zr-rich regions. However, with the EXAFS technique giving only an average of the local structure, we cannot conclude on the Zr concentration in the Zr-rich regions, and hence on the sizes of these regions.

In summary, in all the BTZ relaxors investigated the shape of a ZrO_6 octahedra depends on the nature of its neighboring octahedra (ZrO_6 or TiO_6), the oxygen atoms being differently off-centered with respect to the Zr-Zr and Zr-Ti bonds. The Zr-Zr and Zr-Ti distances do not depend on x, Zr-Ti distances being significantly shorter than Zr-Zr ones. The Zr-Ba bond length increases with the Zr content, and is affected by a strong static disorder. Finally, the EXAFS analysis reveals a tendency of Zr atoms to segregate. Note that in the case of $BaTi_{0.65}Zr_{0.35}O_3$, the Zr environment is found to be remarkably stable with temperature. Therefore, no important changes of the local structure are observed around Zr atoms in the temperature range of the maximum of the dielectric permittivity.

IV. CONCLUDING DISCUSSION

A. Microstructural picture of BTZ relaxors

In the preceding sections we have described quantitatively the local structural features of the Zr environment in BTZ relaxors. It is now interesting to discuss how this local structure contrasts with the average, long-range cubic structure evidenced by x-ray diffraction (XRD). The interatomic distances deduced from EXAFS are compared to those determined from XRD in Fig. 12. The two techniques yield quite different values of distances. On the one hand, the XRD measurements show that the unit cell dimensions of BTZ samples follow the Vegard's law, i.e., the cell volume cubic root linearly increases from its value in $BaTiO_3$ to that in $BaZrO_3$. In the cubic relaxor samples, all the average distances then linearly increase with the Zr substitution rate x. On the other hand, the distances deduced from the EXAFS analysis systematically exceed those expected in the average structure and, with the exception of the Zr-Ba distance, are found to be independent of x. Considering that EXAFS probes the structure on a very local scale, the latter observation is a direct evidence that the local structure is different from the average structure.

We have shown in Sec. III D 3 that Zr atoms tend to segregate in BTZ relaxors. The latter result is in agreement with previous speculations based on Raman scattering.[25] If we assume that the Zr-rich regions consist of $BaZrO_3$ spherical inclusions in a $BaTiO_3$ matrix, it is possible to roughly estimate the mean number of segregated atoms, as well as the size of the inclusions. Pure $BaZrO_3$ regions with radii of a', $a'\sqrt{2}$, $a'\sqrt{3}$, and $2a'$ were considered ($a'=R_3$ is the Zr-Zr distance given in Table IV). These inclusions contain 7, 19, 27, and 33 Zr atoms, respectively. The number of Zr neighbors was determined for each of these Zr atoms, and averaged on the inclusions. The average number of Zr neighbors of one Zr atom is found to be equal to 1.7, 3.2, 3.4, and 3.6 in the spherical inclusions with radii of a', $a'\sqrt{2}$, $a'\sqrt{3}$, and $2a'$, respectively. The latter values can directly be compared

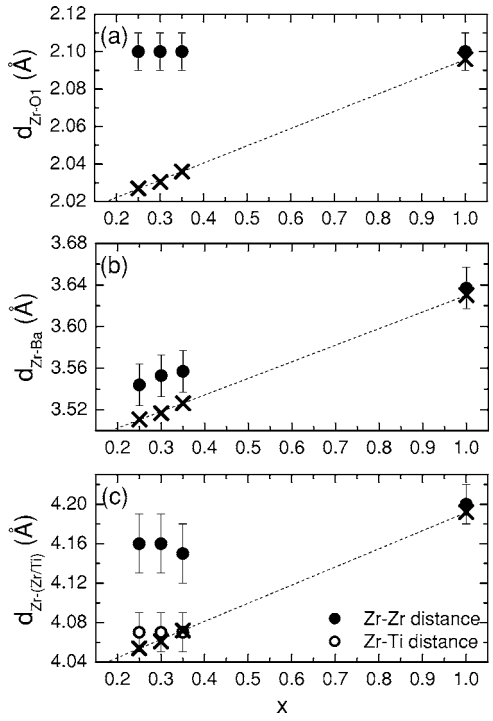

FIG. 12. Evolution of the Zr-O1 (a), Zr-Ba (b), and Zr-(Zr/Ti) (c) distances with the Zr substitution rate x. EXAFS results are reported as round dots. They are compared to the corresponding average distances deduced from the x-ray diffraction experiments (crosses); i.e., $a/2$, $a\sqrt{3}/2$, and a, respectively, where a is the cubic cell parameter.

to N_{Zr}, the mean number of Zr atoms around one Zr atom deduced from the EXAFS analysis. From Table IV, we conclude that the mean number of Zr atoms segregated in hypothetical spherical $BaZrO_3$ regions would be 27 in BTZ with $x=0.35$, corresponding to a radius of $a'\sqrt{3}=7.2$ Å. Concerning BTZ samples with $x=0.30$ and 0.25, linear interpolations on the values enumerated above result in regions of mean radii 5.8 Å (19 Zr atoms) and 5.3 Å (15 Zr atoms), respectively.

The EXAFS study of BTZ relaxors at the Zr K edge thus allowed us to evidence local structural deviations from the average cubic structure, as well as chemical inhomogeneities. In the following, we shall propose a microstructural picture of BTZ relaxors and discuss its origin and implications on the relaxor behavior. In order to expose the possible basic physical mechanisms in a clear and simple manner, we will assume that the segregation of Zr atoms consists of small inclusions of $BaZrO_3$ (non-necessarily spherical) in a $BaTiO_3$ matrix. However, let us recall that the real repartition of the Zr atoms could be much more complex (see Sec. III D 3).

Such $BaZrO_3$ inclusions in BTZ relaxors must be submitted to a chemical pressure from the $BaTiO_3$ environment, which has a smaller unit cell volume than $BaZrO_3$. It is first interesting to note that the Zr-O distance in BTZ relaxors is almost insensitive to this chemical pressure, since it is the same as in $BaZrO_3$ [Fig. 12(a)]. On the other hand, the Zr-Ba distance decreases with increasing Ti content [Fig. 12(b)] and hence, is more sensitive to the chemical pressure. This latter difference in ABO_3 perovskites is well understood within the polyhedral approach: the A-O distance in perovskites is generally more compressible than the shorter B-O distance in the closed-packed BO_6 octahedra.[54] Insight into the BO_6 linkage can be also gained from the $\widehat{ZrO1Zr}$ angle value, which deviates considerably from 180° (Table IV). In a perovskite structure, the presence of buckled Zr-O-Zr bonds suggests the presence of octahedron tilts. This distortion could be a direct consequence of the chemical pressure exerted by the surrounding $BaTiO_3$ matrix. Within this context, let us be reminded that the hydrostatic pressure reveals and/or enhances structural lattice instabilities related to tilts in the perovskite compounds with BO_6 polyhedra more rigid than AO_{12} ones.[55] Furthermore, it has been proposed in the literature that $BaZrO_3$ undergoes a pressure-induced phase transition to the tilted $a^-a^-a^-$ perovskite structure[56] (Glazer's notations[57]). Assuming that the $BaZrO_3$ inclusions adopt the latter structure in BTZ relaxors, the tilt angle calculated from the buckling angle of the Zr-O-Zr bonds is about 11°, which is a reasonable value for a tilted perovskite.[58–60] In summary, within our simplified picture, $BaZrO_3$ inclusions do not adopt the cubic bulk structure of $BaZrO_3$ but present considerable distortions away from it. The Zr environment in BTZ relaxors appears to be determined by both the high stiffness of the ZrO_6 octahedra and chemical pressure effects.

Let us now discuss the structure around the inclusions. Given that the Zr-Zr distance is approximately 2% larger than the average B-B cation distance deduced from XRD [Fig. 12(c)], we expect a significant strain at the interface of the $BaZrO_3$ inclusions and the $BaTiO_3$ matrix. The TiO_6 octahedra adjacent to the inclusions likely accommodate the structural misfit between $BaZrO_3$ inclusions and the $BaTiO_3$ matrix. Considering that the cell volume of $BaZrO_3$ is larger than that of $BaTiO_3$, we expect that these adjacent TiO_6 octahedra are then submitted to a tensile strain. Although their deformation shape remains an open question, different Ti^{4+} displacements (and thus polarity) are expected in the adjacent regions when compared to the $BaTiO_3$ matrix. These displacements, which depend on local strain, would naturally lead to random electric fields. Note that the important impact of the local chemical environment has already been evoked for the solid solution $Pb(Sc,Ta)O_3$-$PbTiO_3$ (PST-PT).[39]

B. Comparison to PZT

We have already mentioned in the Introduction that the ferroelectric $PbZr_{1-x}Ti_xO_3$ (PZT), similar to BTZ, does surprisingly present no relaxation, making the comparison of BTZ to PZT insightful. First, we note that in both BTZ and PZT, the mean Zr-O distance is almost unaffected by the Ti content, and equal to 2.07–2.08 Å within the data accuracy, which is very close to the Zr-O distance in BTZ and $BaZrO_3$ (2.10 Å).[33] As a consequence, the relaxor properties of BTZ cannot only be linked to the stiffness of ZrO_6 octahedra.

It is obvious that the presence of either Ba^{2+} or Pb^{2+} cations, which show very dissimilar electronic configurations, can drive the different properties of BTZ and PZT. However, an explanation for the different behaviors of BTZ and PZT could lie in the local chemical order, which is known to play

a determinant role for relaxor properties (e.g., the so-called 1:1 Mg/Nb order on the nanometer scale in PMN).[10,11] In that context, it is interesting to note that BTZ cannot be synthesized in the region $0.5<x<1$ (Ref. 7), which suggests an important internal chemical strain which inhibits the formation of BTZ across the whole composition range. We speculate that the local phase segregation observed for BTZ relaxors is a precursor for the macroscopic phase separation observed for higher Zr substitution rates. Such an internal chemical strain does not seem to exist for PZT since it forms a solid solution whatever the Zr/Ti ratio. The distribution of elastic fields is thus expected to differ significantly from BTZ to PZT. In particular, the strain around the local phase separation in BTZ can be regarded as the source of random elastic fields. Such random elastic fields are then considered to lead to a particular local pattern of polar regions and thus random electric fields, that cause the relaxor behavior.

ACKNOWLEDGMENTS

We are indebted to O. Proux (LGIT) for his help during the EXAFS experiments. This work was supported by an ACI project of the French ministry of research, and has been conducted within the framework of the European network of excellence FAME.

*Electronic address: jens.kreisel@inpg.fr

[1] P. W. Rehrig, S. E. Park, S. Trollier-McKinstry, G. L. Messing, B. Jones, and T. R. Shrout, J. Appl. Phys. **86**, 1657 (1999).
[2] Z. Yu, R. Guo, and A. S. Bhalla, Appl. Phys. Lett. **77**, 1535 (2000).
[3] Z. Yu, C. Ang, R. Guo, and A. S. Bhalla, J. Appl. Phys. **92**, 1489 (2002).
[4] T. B. Wu, C. M. Wu, and M. L. Chen, Thin Solid Films **334**, 77 (2003).
[5] V. Reymond, S. Payan, D. Michau, J. P. Manaud, and M. Maglione, Thin Solid Films **467**, 54 (2004).
[6] Y. Hotta, G. W. J. Hassink, T. Kawai, and H. Tabata, Jpn. J. Appl. Phys., Part 1 **42**, 5908 (2003).
[7] J. Ravez and A. Simon, Eur. J. Solid State Inorg. Chem. **34**, 1199 (1997).
[8] S. E. Park and T. R. Shrout, J. Appl. Phys. **82**, 1804 (1997).
[9] Y.-M. Chiang, G. W. Farrey, and A. N. Soukhojak, Appl. Phys. Lett. **73**, 3683 (1998).
[10] L. E. Cross, Ferroelectrics **76**, 241 (1987).
[11] L. E. Cross, Ferroelectrics **151**, 305 (1994).
[12] G. A. Samara, J. Phys.: Condens. Matter **15**, R367 (2003).
[13] G. A. Samara and E. L. Venturini, Phase Transitions **79**, 21 (2006).
[14] B. Noheda and D. E. Cox, Phase Transitions **97**, 5 (2006).
[15] V. Westphal, W. Kleemann, and M. D. Glinchuk, Phys. Rev. Lett. **68**, 847 (1992).
[16] G. Burns and F. H. Dacol, Solid State Commun. **48**, 853 (1983).
[17] P. Bonneau, P. Garnier, G. Calvarin, E. Husson, J. R. Gavarri, A. W. Hewat, and A. Morell, J. Solid State Chem. **91**, 350 (1991).
[18] N. de Mathan, E. Husson, G. Calvarin, and J. R. Gavarri, J. Phys.: Condens. Matter **3**, 8159 (1991).
[19] S. Vakhrushev, A. Nabereznov, S. K. Sinha, Y. P. Feng, and T. Egami, J. Phys. Chem. Solids **57**, 1517 (1996).
[20] B. Chaabane, J. Kreisel, B. Dkhil, P. Bouvier, and M. Mezouar, Phys. Rev. Lett. **90**, 257601 (2003).
[21] G. Xu, G. Shirane, J. R. D. Copley, and P. M. Gehring, Phys. Rev. B **69**, 064112 (2004).
[22] I. K. Jeong, T. W. Darling, J. K. Lee, T. Proffen, R. H. Heffner, J. S. Park, K. S. Hong, W. Dmowski, and T. Egami, Phys. Rev. Lett. **94**, 147602 (2005).
[23] R. Farhi, M. El Marssi, A. Simon, and J. Ravez, Eur. Phys. J. B **18**, 605 (2000).
[24] R. Farhi, M. El Marssi, A. Simon, and J. Ravez, Eur. Phys. J. B **9**, 599 (1999).
[25] J. Kreisel, P. Bouvier, M. Maglione, B. Dkhil, and A. Simon, Phys. Rev. B **69**, 092104 (2004).
[26] P. Sciau, G. Calvarin, and J. Ravez, Solid State Commun. **113**, 77 (2000).
[27] A. Simon, J. Ravez, and M. Maglione, J. Phys.: Condens. Matter **16**, 963 (2004).
[28] B. Noheda, Curr. Opin. Solid State Mater. Sci. **6**, 27 (2002).
[29] B. Ravel, E. A. Stern, R. I. Vedrinskii, and V. Kraizman, Ferroelectrics **206**, 407 (1998).
[30] O. Hanske-Petitpierre, Y. Yacoby, J. Mustre de Leon, E. A. Stern, and J. J. Rehr, Phys. Rev. B **44**, 6700 (1991).
[31] A. I. Frenkel, F. M. Wang, S. Kelly, R. Ingalls, D. Haskel, E. A. Stern, and Y. Yacoby, Phys. Rev. B **56**, 10869 (1997).
[32] N. Sicron, B. Ravel, Y. Yacoby, E. A. Stern, F. Dogan, and J. J. Rehr, Phys. Rev. B **50**, 13168 (1994).
[33] D. Cao, I.-K. Jeong, R. H. Heffner, T. Darling, J.-K. Lee, F. Bridges, J.-S. Park, and K.-S. Hong, Phys. Rev. B **70**, 224102 (2004).
[34] E. Prouzet, E. Husson, N. de Mathan, and A. Morell, J. Phys.: Condens. Matter **5**, 4889 (1993).
[35] I. W. Chen, P. Li, and Y. Wang, J. Phys. Chem. Solids **57**, 1525 (1996).
[36] V. A. Shuvaeva, I. Pirog, Y. Azuma, K. Yagi, K. Sakaue, H. Terauchi, I. P. Raevski, K. Zhuchkov, and M. Y. Antipin, J. Phys.: Condens. Matter **15**, 2413 (2003).
[37] V. A. Shuvaeva, Y. Azuma, I. P. Raevski, K. Yagi, K. Sakaue, and H. Terauchi, Ferroelectrics **299**, 103 (2004).
[38] V. A. Shuvaeva, D. Zekria, A. M. Glazer, Q. Jiang, S. M. Weber, P. Bhattacharya, and P. A. Thomas, Phys. Rev. B **71**, 174114 (2005).
[39] A. I. Frenkel, D. M. Pease, J. Giniewicz, E. A. Stern, D. L. Brewe, M. Daniel, and J. Budnick, Phys. Rev. B **70**, 014106 (2004).
[40] B. Ravel, C. E. Bouldin, H. Renevier, J.-L. Hodeau, and J.-F. Bérar, Phys. Rev. B **60**, 778 (1999).
[41] M. Newville, P. Livins, Y. Yacoby, J. J. Rehr, and E. A. Stern, Phys. Rev. B **47**, 14126 (1993).
[42] S. I. Zabinsky, J. J. Rehr, A. Ankudinov, R. C. Albers, and M. J. Eller, Phys. Rev. B **52**, 2995 (1995).
[43] M. Newville, B. Ravel, D. Haskel, J. J. Rehr, E. A. Stern, and Y.

Yacoby, Physica B **208-209**, 154 (1995).
[44] A. L. Ankudinov, B. Ravel, J. J. Rehr, and S. D. Conradson, Phys. Rev. B **58**, 7565 (1998).
[45] D. Haskel, B. Ravel, M. Newville, and E. A. Stern, Physica B **208-209**, 151 (1995).
[46] L. A. Bugaev, V. A. Shuvaeva, I. B. Alekseenko, and R. V. Vedrinskii, Physica B **208-209**, 169 (1995).
[47] P. E. Petit, F. Guyot, and F. Farges, J. Phys. IV **7**, C2-1065 (1997).
[48] Actually, small local deviations from a perfect cubic structure do exist in $BaZrO_3$, as shown by the existence of a weak first-order Raman spectrum [see C. Chemarin *et al.*, J. Solid State Chem. **149**, 298 (2000)]. Our purpose being to set reference parameters for the analysis of BTZ, these minor distortions can be safely neglected here.
[49] M. D. Mathews, E. B. Mirza, and A. C. Momin, J. Mater. Sci. Lett. **10**, 305 (1991).
[50] I. Levin, T. G. Amos, S. M. Bell, L. Farber, T. A. Vanderah, R. S. Roth, and B. H. Toby, J. Solid State Chem. **175**, 170 (2003).
[51] Different energy shifts ΔE_{0_i} could have been introduced for each of the SS paths, in order to compensate for slight inadequancies of the calculated phase shifts (Ref. 45). We do not use this method, our aim being to compare the distances obtained in $BaZrO_3$ and BTZ samples. In the case of BTZ relaxors indeed, the complexity of the fit is such that these additional parameters cannot be meaningful.
[52] A. Frenkel, E. A. Stern, A. Voronel, M. Qian, and M. Newville, Phys. Rev. B **49**, 11662 (1994).
[53] G. H. Kwei, A. C. Lawson, S. J. L. Billinge, and S. W. Cheong, J. Phys. Chem. **97**, 2368 (1993).
[54] R. M. Hazen and L. W. Finger, *Comparative Crystal Chemistry* (Wiley, New York, 1982).
[55] R. J. Angel, J. Zhao, and N. L. Ross, Phys. Rev. Lett. **95**, 025503 (2005).
[56] C. Chemarin, N. Rosman, T. Pagnier, and G. Lucazeau, J. Solid State Chem. **149**, 298 (2000).
[57] A. M. Glazer, Acta Crystallogr., Sect. B: Struct. Crystallogr. Cryst. Chem. **28**, 3384 (1972).
[58] R. H. Mitchell, *Perovskites—Modern and Ancient* (Almaz Press, Thunder Bay, 2002).
[59] K. A. Müller, W. Berlinger, and F. Waldner, Phys. Rev. Lett. **21**, 814 (1968).
[60] G. Roult, R. Pastuszak, R. Marchand, and Y. Laurent, Acta Crystallogr., Sect. C: Cryst. Struct. Commun. **39**, 673 (1983).